Dynamics of particle network in composite battery cathodes

Authors: Jizhou Li[1†], Nikhil Sharma[2†], Zhisen Jiang[1], Yang Yang[3‡], Federico Monaco[3], Zhengrui Xu[4], Dong Hou[4], Daniel Ratner[5], Piero Pianetta[1], Peter Cloetens[3], Feng Lin[4*], Kejie Zhao[2*], Yijin Liu[1*]

Affiliations:

[1] Stanford Synchrotron Radiation Lightsource, SLAC National Accelerator Laboratory; Menlo Park, CA 94025, USA

[2] School of Mechanical Engineering, Purdue University; West Lafayette, IN 47906, USA

[3] European Synchrotron Radiation Facility; Grenoble 38000, France

[4] Department of Chemistry, Virginia Tech; Blacksburg, VA 24061, USA

[5] Machine Learning Initiative, SLAC National Accelerator Laboratory; Menlo Park, CA 94025, USA

[†] These authors contributed equally to this work: Jizhou Li, Nikhil Sharma

[‡] Present address: National Synchrotron Light Source II, Brookhaven National Laboratory; Upton, New York 11973, USA

[*] Corresponding author. Email: F. Lin (fenglin@vt.edu), K. Zhao (kjzhao@purdue.edu), and Y. Liu (liuyijin@slac.stanford.edu)

Abstract: Improving composite battery electrodes requires a delicate control of active materials and electrode formulation. The electrochemically active materials are often in the form of micron-sized particles, which fulfill their role as energy exchange reservoirs through interacting with the surrounding conductive network. A network evolution model is formulated here to interpret the regulation and equilibration between electrochemical activity and mechanical damage of these particles. Through statistically analyzing thousands of particles in a $LiNi_{0.8}Mn_{0.1}Co_{0.1}O_2$-based cathode, we found that the local network heterogeneity results in asynchronous activities in the early cycles, and later the particle assemblies move toward a synchronous behavior. Our study pinpoints the chemomechanical behavior of individual particles and enables better designs of the conductive network to optimize the utility of all the particles during operation.

One-Sentence Summary: Active particles in composite electrodes initially show asynchronous activity that evolves towards synchronous behavior.

Main Text:

Lithium-ion batteries (LIBs), with high energy density and long lifetime, are widely adopted for a broad range of applications. LIB's composite cathode is made of many electrochemically active particles embedded in a conductive carbon and binder matrix. The microstructure plays a crucial role in governing the LIB performance through modulating the electronic/ionic transport properties (*1*, *2*) and the chemomechanical behavior (*3–5*). The cracking, disintegration, and (de)activation behaviors of the electrochemically active cathode particles affect the capacity fade over prolonged battery cycling (*6*, *7*).

Alleviation of the active particle damage has focused on tuning the morphological characteristics of individual particles, such as size, sphericity, elongation, etc (*8–16*). For instance, reducing the primary particle size is an effective approach to improving the fast-charging performance because smaller particles have shorter ion diffusion paths (*17–19*). Designing particles with elongated morphology, e.g., in the form of nanoplates or nanorods, can also improve the specific capacity and reduce charge transfer resistance (*20*). However, the correlation between the particle morphology and the cell performance is rather complex with effects at multiple length and time scales. The dynamics of particle network have significant impacts but are rarely studied. For example, recent studies have uncovered the local heterogeneity in the electrode, where active particles contribute to the cell-level chemistry differently in time and position (*21*). Some particles release lithium ions at a faster rate than their peers under fast charging conditions (*22*). Some local regions could become inactive while the cell can still function well as a whole. To make a substantial improvement effectively, the particle structure and the electrode morphology shall be tailored coherently and a synergy could be achieved by doing so.

This study aims to formulate an in-depth understanding of the dynamically evolving cathode particle disintegration, both individually and collectively. We reveal that, although it seems that a global homogenization will be developed eventually after long-term cycling, a poorly designed electrode would reach this state when most of its particles are severely damaged. In contrast, a well-formed electrode would rapidly converge to the electrode synchronization with majority of its particles still in good shape. In our study, we image thick Ni-rich composite cathode electrodes with multi-layer of $LiNi_{0.8}Mn_{0.1}Co_{0.1}O_2$ (NMC) particles at different states using nano-resolution hard X-ray phase contrast holo-tomography (**Fig. 1A**). These electrodes are recovered from standard coin cells that were cycled under fast-charging conditions for 10 cycles and 50 cycles, respectively. With high spatial resolution, exceptional contrast, and a large field of view, our three-dimensional imaging data covers a large number of active particles that demonstrate a wide variety of damage patterns. To facilitate a statistical analysis, we build on our previous neural network-based particle identification method (*1*) and significantly improve its accuracy and efficiency by developing a diagonal data fusion approach, which is illustrated in **Figs. S1** and **S2**. Upon completion of the particle identification using this method, the damage level of individual particle is further quantified. The relative probability distribution of the particle damage degree is presented in **Fig. 1B**, and a few randomly selected particles with different damage patterns are highlighted in **Fig. 1C-1F.**

The severely damaged particles are those being overused during the electrochemical fast-charging process. Their spatial distribution and arrangement are evidence of the spatially heterogeneous electrode utility. As shown in **Figs. 2A** and **2B**, the severely damaged particles are sparsely distributed in the 10-cycled electrode and, their concentration increased upon further

cycling, featuring a denser agglomeration in the 50-cycled electrode (as illustrated in the enlarged views). **Fig. 2C** shows the probability distributions of the distance between two neighboring severely damaged particles in 10-cycled and 50-cycled electrodes, respectively. A shift towards shorter distance can be observed in the 50-cycled electrode, indicating a synchronization effect within the local particle clusters.

We perform theoretical modeling to understand the damage and Li reactions behaviors of NMC particles across cycles. We envision that the interplay between the electrochemical activity and the mechanical damage regulates the performance of the NMC particles – while the deeper state of charge incurs more severe consequences such as the particle damage and decohesion of particles from the conductive agent, the mechanical damage increases the cost of Li reactions and suppresses the electrochemical activity of individual particles. A more synchronous behavior of the composite cathode is achieved in the prolonged cycles due to the equilibrium between the electrochemical activity and mechanical damage. To test this hypothesis, we conduct finite element analysis to model the electrochemical response and mechanical damage of a NMC cathode composed of three spherical NMC active particles surrounded by two homogenous porous carbon/binder (CB) domains of different electrical conductivities (**Fig. 3**). We stress that the intention of the computational model is not to capture all the explicit microstructural details in the composite cathode. Rather, our goal is to replicate the salient feature in the composite that the active NMC particles are covered by different degrees of the electrically conductive agent, which results in the various local conducting network for individual particles. In this simplified model, the surrounding high conductivity and low conductivity CBs differ in their electrical conductivities. The model assumes that liquid electrolyte is soaked in the porous CB domains and thus the NMC particles are fully accessible to the Li^+ in the liquid electrolyte. We set different ratios of coverage of CB on the periphery of each active particle, as illustrated in **Fig. 3A**. The interface of active particles attached to the high conductivity CB undergoes a faster electrochemical reaction than the boundary enclosed by the low conductivity CB. Thus, each active particle experiences dissimilar network electrochemical activities, as inferred from the diverging concentration profiles (C/C_{max}) during the 1st charging process (**Fig. 3B**).

The modulation between the electrochemical activity and mechanical damage reduces the variation of Li concentration with the progression of (dis)charge cycles. As shown in the normalized Li concentration plot (**Fig. 3B**) and the plot of the Li concentration variation across the three NMC particles (**Fig. 3C**), the concentration profiles converge with battery operation. During the charging process, Li extraction generates a reduction of the lattice volume in the NMC particles (*25*). Considerable variation in the mechanical properties of the NMC particles (elastic Modulus = 140 GPa) and CB (elastic Modulus = 2 GPa) generates strain mismatch at the interface. The apex of the mismatch occurs near the end of the charging process, demonstrated by the divergence of the damage profiles in **Fig. 3D** and their corresponding differences to the mean damage in **Fig. 3E**.

After the onset of heterogeneous damage among the NMC particles, the individual damage curves diverge (**Fig. 3D**). The individual NMC particle characteristic, i.e., the dissimilar coverage by high and low conductivity CBs, commands the degree of heterogeneous damage in the early cycles. With successive discharging and charging processes, the modulation between electrochemical activity and mechanical damage reduces the imbalance within the system (through the interfacial resistance for charge transfer). Consequently, the damage level for all the three particles converges, demonstrating the system's progression towards a synchronized

behavior. In addition, we observe a similar transformation to synchronized damage behavior for the system with more NMC active particles (**Fig. S4**). The variation in the periphery contact with high and low conductivity CB regions generates heterogeneous reactions for each particle. After the initial divergence, the individual particle damage is tuned by the feedback to electrochemical activity that culminates towards a synchronized behavior in the composite electrode.

Both the particle damage and Li concentration profiles theoretically confirm the asynchronous to synchronous evolution in composite cathodes. Such transition can occur for a number of reasons, such as from the particles' self-attributes, interactions with neighboring particles and CB domains. To probe the evolution mechanisms from the intrinsic or internal physical nature of cathode particles, the 3D tomographic imaging data is analyzed through an interpretable machine learning framework.

Using the over 2000 accurately identified NMC particles, we extract their structural, chemical, and morphological characteristics. More specifically, we divide the particle attributes into four different groups: position, chemical properties, particle structure, and local morphology (as illustrated in **Figs. S5** and **S6**, in total 24 attributes are extracted). As indicated in **Fig. S7**, these extracted particle attributes demonstrate varying characteristics in their respective probability distributions. Revealing their interrelationship is not straightforward and could benefit from more advanced computing and modeling approaches.

We leverage the advances in machine learning to model relationship and dependencies among attributes, i.e. descriptors of the cathode particles properties (**Fig. S8**). The model has to be both accurate and interpretable. To elucidate the intertwined limiting factors for battery cathode robustness, the degree of cathode NMC particles' engagement in the cell level chemistry is explored through attribute correlation and damage regression. These two steps are accomplished using a regularized autoencoder neural network (*26*) and random forest (RF) regression (*27*). The SHAP (SHapley Additive exPlanations) (*28*) is utilized to rank the significance of the particle properties to the degree of particle damaging during the process of regression, which effectively reveals the contributions of different microstructural characteristics to the damage profile for every single particle in our electrode. The Circular plot (*29*) is used for better visualization of the Pearson's correction among different particle attributes. Integrated with the SHAP values, the RF provides not only accurate regression results, but also the interpretability of the impacts of all the input attributes on individual predictions as well as global insights.

Specifically, the autoencoder neural network compresses the input attributes into latent dimension (LDs) via an encoder network, which has been extensively applied for scientific discovery due to its ability to learn non-linear functions and its good interpretability (*30*, *31*). The LDs of both datasets for 10-cycled and 50-cycled electrodes, respectively, are calculated and are subsequently correlated with each other through Pearson's correlation. As shown in **Figs. 4A** and **4B**, different LDs show intertwined relationship in both cases. Each node in the circular plot represents one LD and a connection between two nodes indicates a relatively high correlation between them. The sign of the correlation coefficient (+/-) defines the direction of the relationship. For the 10-cycled electrode, the first five LDs appear to be independent. As more LDs are added, we start to observe correlations among them. For the 50-cycled electrode, in addition to the common connections, several additional correlations emerge (as highlighted by dark colors in **Fig. 4B**). The observation of a higher degree of interdependence among different

LDs indicates that the particles' structural and chemical characteristics become more intertwined upon battery cycling.

When interpreting the model regression results with the SHAP values, which utilizes the game-theory-based Shapley values (*32*), the contribution of each attribute to the model's output (the particle damage degree) can be obtained. Attributes with larger SHAP values are considered to be more important to the target damage degree. The contribution scores of all attributes to the particle damage in both 10-cycled and 50-cycled electrodes are presented in **Fig. 4C** (attributes are grouped based on their properties and reordered for better visualization) and the interpretation is provided below. The advantage of using SHAP to explain the regression model is its superior robustness to correlated attributes compared to the traditional methods (*33*), e.g., the Pearson's correlation, which cannot systematically capture the key differences in the studied electrodes (**Fig. S11**).

From our model-based prediction in **Fig. 4C,** some of the attributes follow expected trends. For example, the particle's depth, *Z*, has a role to play in affecting the particle damage (*21*, *34*). This can be related to the cell polarization effect, which results in the fact that particles at different depth are effectively experiencing different state of charge at a given time. The *Z*-dependence of particle damage is more significant in the 10-cycled electrode, in good agreement with previous reports (*1*, *21*). The electron density, *EDensity*, has been associated with the state of charge (*1*) and its averaged value and degree of variation, *Homogeneity*, shows considerable impact on the particle damage throughout the cycling process. The surface area and roughness (*RoughOuter*, *RoughInner*, *SurfOuter*, and *SurfInner*) could affect the cohesion of the active particles and the CB matrix. Therefore, the surface characteristics could have a role to play. The particle's size, *Volume*, appears to be correlated with the particle damage. Its contribution score seems slightly lower in the 50-cycled electrode. This trend suggests that the particle size effect might not be the limiting factor in the later cycles. However, the variation of the neighboring particles' volumes, *VolumeStd*, shows an opposite trend, featuring a higher contribution score in the 50-cycled electrode. This observation indicates that, upon prolonged battery operation, the uniformity in the neighboring particle size becomes a more significant factor that would affect the particle damage. Mixing particles with different size has been utilized as a method to improve the electrode's packing density. Our result suggests that this approach shall be carefully examined from the long-term cyclability perspective. Another finding is that the particle elongation, *Elongation*, has a rather significant contribution score, which, however, decreases upon cycling. On the other hand, the alignment of the neighboring particles, *OrienIso*, which shows negligible contribution in the 10-cycled electrode, becomes significant in the later cycles. In advanced battery electrode manufacturing, the particle alignment can be purposely adjusted by controlling the externally applied electric and/or magnetic fields (*35–37*).

When visualizing the overall picture of our statistical analysis over thousands of particles, we reveal an interesting pattern: in the early cycles, individual particles' characteristics (e.g. the position *Z*, *VSratio, Sphericity,* and *Elongation*) predominantly determine their respective degrees of damage, featuring an asynchronous behavior that is in agreement with our theoretical modeling result. In the later cycles, however, the interplay among neighboring particles (e.g. *Contact*, *DisNearest*, *OrienIso*, and *PDensity*) becomes more important, which indicates that the local inter-particle arrangement can critically impact the asynchronous-to-synchronous transition. The mean difference and standard deviation of each attribute's contribution scores

between the 10-cycled and 50-cycled datasets is present on the top of **Fig. 4C,** featuring a valley on the left and a peak on the right, supporting the above-described observation.

Our experimental observations (**Fig. 2**) and machine learning analysis (**Fig. 4**) collectively corroborate with the theoretical modeling (**Fig. 3**). These results reveal a transition from the asynchronous behavior in the early stage toward a synchronous state later in the particle network evolution, where the interplay among neighbor particles plays a facilitating role (**Fig. S12**). Particles' self-attributes together with the dynamic nature of the conductive network jointly determine the damage behavior of NMC particles in composite electrodes. These are critical factors for cathode design to prolong the cycle life of batteries. Based on our results, in the active cathode powder, it is useful to suppress the particle-to-particle variation in their structural characteristics, such as particle size, sphericity, elongation etc. At the electrode scale, an ordered particle arrangement is favorable, which can be reinforced through a field-guided approach. While the in-plane homogeneity is desirable, in the out-of-plane direction, a structural gradient could be beneficial due to the electrochemical polarization, which is more severe in thick electrodes. To summarize, an ordered electrode configuration with tailored depth-dependent packing of uniform active particles would be robust to prolonged battery cycling.

From the synthesis perspective, the particle shape and structure can be tuned by controlling the sintering temperature, incorporation of trace element doping, designing the architecture of the precursor, and surface coating. These are common synthesis strategies and can be scalable for mass production. For the electrode manufacturing, the field-guided approach has been demonstrated to be effective for creating an ordered structure. This is compatible with the existing electrode manufacturing facilities and, thus, can be fairly cost effective.

References and Notes

1. Z. Jiang, J. Li, Y. Yang, L. Mu, C. Wei, X. Yu, P. Pianetta, K. Zhao, P. Cloetens, F. Lin, Y. Liu, Machine-learning-revealed statistics of the particle-carbon/binder detachment in lithium-ion battery cathodes. *Nature Communications*. 11, 2310 (2020).

2. D. E. Stephenson, B. C. Walker, C. B. Skelton, E. P. Gorzkowski, D. J. Rowenhorst, D. R. Wheeler, Modeling 3D Microstructure and Ion Transport in Porous Li-Ion Battery Electrodes. *J Electrochem Soc*. 158, A781 (2011).

3. R. Xu, Y. Yang, F. Yin, P. Liu, P. Cloetens, Y. Liu, F. Lin, K. Zhao, Heterogeneous damage in Li-ion batteries: Experimental analysis and theoretical modeling. *J Mech Phys Solids*. 129, 160–183 (2019).

4. L. Mu, Z. Yang, L. Tao, C. K. Waters, Z. Xu, L. Li, S. Sainio, Y. Du, H. L. Xin, D. Nordlund, F. Lin, The sensitive surface chemistry of Co-free, Ni-rich layered oxides: identifying experimental conditions that influence characterization results. *J Mater Chem A*. 8, 17487–17497 (2020).

5. Z. Yang, L. Mu, D. Hou, M. M. Rahman, Z. Xu, J. Liu, D. Nordlund, C. Sun, X. Xiao, F. Lin, Probing Dopant Redistribution, Phase Propagation, and Local Chemical Changes in the Synthesis of Layered Oxide Battery Cathodes. *Adv Energy Mater*. 11, 2002719 (2021).

6. Z. Yang, F. Lin, Heterogeneous, Defect-Rich Battery Particles and Electrodes: Why Do They Matter, and How Can One Leverage Them? *J Phys Chem C*. 125, 9618–9629 (2021).

7. Z. Xu, D. Hou, D. J. Kautz, W. Liu, R. Xu, X. Xiao, F. Lin, Charging Reactions Promoted by Geometrically Necessary Dislocations in Battery Materials Revealed by In Situ Single Particle Synchrotron Measurements. *Adv Mater*. 32, 2003417 (2020).

8. F. Lin, K. Zhao, Y. Liu, Heterogeneous Reaction Activities and Statistical Characteristics of Particle Cracking in Battery Electrodes. *Acs Energy Lett*. 6, 4065–4070 (2021).

9. W. Li, E. M. Erickson, A. Manthiram, High-nickel layered oxide cathodes for lithium-based automotive batteries. *Nat Energy*. 5, 26–34 (2020).

10. Z. Xu, Z. Jiang, C. Kuai, R. Xu, C. Qin, Y. Zhang, M. M. Rahman, C. Wei, D. Nordlund, C.-J. Sun, X. Xiao, X.-W. Du, K. Zhao, P. Yan, Y. Liu, F. Lin, Charge distribution guided by grain crystallographic orientations in polycrystalline battery materials. *Nat Commun*. 11, 83 (2020).

11. H. H. Sun, H.-H. Ryu, U.-H. Kim, J. A. Weeks, A. Heller, Y.-K. Sun, C. B. Mullins, Beyond Doping and Coating: Prospective Strategies for Stable High-Capacity Layered Ni-Rich Cathodes. *Acs Energy Lett*. 5, 1136–1146 (2020).

12. Z. Zhu, D. Yu, Y. Yang, C. Su, Y. Huang, Y. Dong, I. Waluyo, B. Wang, A. Hunt, X. Yao, J. Lee, W. Xue, J. Li, Gradient Li-rich oxide cathode particles immunized against oxygen release by a molten salt treatment. *Nat Energy*. 4, 1049–1058 (2019).

13. W. E. Gent, Y. Li, S. Ahn, J. Lim, Y. Liu, A. M. Wise, C. B. Gopal, D. N. Mueller, R. Davis, J. N. Weker, J. Park, S. Doo, W. C. Chueh, Persistent State of Charge Heterogeneity in Relaxed, Partially Charged Li1−xNi1/3Co1/3Mn1/3O2 Secondary Particles. *Adv Mater*. 28, 6631–6638 (2016).

14. A. J. Merryweather, C. Schnedermann, Q. Jacquet, C. P. Grey, A. Rao, Operando optical tracking of single-particle ion dynamics in batteries. *Nature*. 594, 522–528 (2021).

15. M. Yoon, Y. Dong, J. Hwang, J. Sung, H. Cha, K. Ahn, Y. Huang, S. J. Kang, J. Li, J. Cho, Reactive boride infusion stabilizes Ni-rich cathodes for lithium-ion batteries. *Nat Energy*. 6, 362–371 (2021).

16. H. H. Sun, U.-H. Kim, J.-H. Park, S.-W. Park, D.-H. Seo, A. Heller, C. B. Mullins, C. S. Yoon, Y.-K. Sun, Transition metal-doped Ni-rich layered cathode materials for durable Li-ion batteries. *Nat Commun*. 12, 6552 (2021).

17. S. Kuppan, Y. Xu, Y. Liu, G. Chen, Phase transformation mechanism in lithium manganese nickel oxide revealed by single-crystal hard X-ray microscopy. *Nat Commun*. 8, 14309 (2017).

18. C. Delacourt, P. Poizot, S. Levasseur, C. Masquelier, Size Effects on Carbon-Free LiFePO[sub 4] Powders. *Electrochem Solid-state Lett*. 9, A352 (2006).

19. L. Bläubaum, F. Röder, C. Nowak, H. S. Chan, A. Kwade, U. Krewer, Impact of Particle Size Distribution on Performance of Lithium Ion Batteries. *Chemelectrochem*. 7, 4755–4766 (2020).

20. D.-H. Kim, J. Kim, Synthesis of LiFePO4 nanoparticles and their electrochemical properties. *J Phys Chem Solids*. 68, 734–737 (2007).

21. Y. Yang, R. Xu, K. Zhang, S. Lee, L. Mu, P. Liu, C. K. Waters, S. Spence, Z. Xu, C. Wei, D. J. Kautz, Q. Yuan, Y. Dong, Y. Yu, X. Xiao, H. Lee, P. Pianetta, P. Cloetens, J. Lee, K. Zhao, F. Lin, Y. Liu, Quantification of Heterogeneous Degradation in Li Ion Batteries. *Adv Energy Mater*. 9, 1900674 (2019).

22. J. Park, H. Zhao, S. D. Kang, K. Lim, C.-C. Chen, Y.-S. Yu, R. D. Braatz, D. A. Shapiro, J. Hong, M. F. Toney, M. Z. Bazant, W. C. Chueh, Fictitious phase separation in Li layered oxides driven by electro-autocatalysis. *Nat Mater*, 1–9 (2021).

23. T. K. Ho, (IEEE, 1995), vol. 1 of *Proceedings of 3rd international conference on document analysis and recognition*, pp. 278–282.

24. S. Lundberg, S.-I. Lee, in *Advances in Neural Information Processing Systems* (2017), *arXiv preprint arXiv:1705.07874*.

25. L. Jingyi, Z. Zhiwei, L. Ziyan, H. Zhenjiang, Z. Junchao, L. Yunjiao, M. Jing, D. Kehua, Microcrack generation and modification of Ni-rich cathodes for Li-ion batteries: A review, e00305.

26. M. A. Kramer, Nonlinear principal component analysis using autoassociative neural networks. *AIChE journal*. 37, 233–243 (1991).

27. L. Breiman, Random forests. *Machine learning*. 45, 5–32 (2001).

28. S. M. Lundberg, G. Erion, H. Chen, A. DeGrave, J. M. Prutkin, B. Nair, R. Katz, J. Himmelfarb, N. Bansal, S.-I. Lee, From local explanations to global understanding with explainable AI for trees. *Nat Mach Intell*. 2, 56–67 (2020).

29. M. Krzywinski, J. Schein, İ. Birol, J. Connors, R. Gascoyne, D. Horsman, S. J. Jones, M. A. Marra, Circos: An information aesthetic for comparative genomics. *Genome Res*. 19, 1639–1645 (2009).

30. R. Gómez-Bombarelli, J. N. Wei, D. Duvenaud, J. M. Hernández-Lobato, B. Sánchez-Lengeling, D. Sheberla, J. Aguilera-Iparraguirre, T. D. Hirzel, R. P. Adams, A. Aspuru-Guzik, Automatic Chemical Design Using a Data-Driven Continuous Representation of Molecules. *Acs Central Sci*. 4, 268–276 (2018).

31. G. Qian, J. Zhang, S.-Q. Chu, J. Li, K. Zhang, Q. Yuan, Z.-F. Ma, P. Pianetta, L. Li, K. Jung, Y. Liu, Understanding the Mesoscale Degradation in Nickel-Rich Cathode Materials through Machine-Learning-Revealed Strain–Redox Decoupling. *Acs Energy Lett*, 687–693 (2021).

32. L. S. Shapley, A value for n-person games. *Contrib. Theor. Games*, 307–317 (1953).

33. S. Lundberg, S.-I. Lee, A unified approach to interpreting model predictions. *arXiv preprint arXiv:1705.07874* (2017).

34. J. Hu, B. Wu, X. Cao, Y. Bi, S. Chae, C. Niu, B. Xiao, J. Tao, J. Zhang, J. Xiao, Evolution of the rate-limiting step: From thin film to thick Ni-rich cathodes. *J Power Sources*. 454, 227966 (2020).

35. J. Billaud, F. Bouville, T. Magrini, C. Villevieille, A. R. Studart, Magnetically aligned graphite electrodes for high-rate performance Li-ion batteries. *Nat Energy*. 1, 16097 (2016).

36. J. S. Sander, R. M. Erb, L. Li, A. Gurijala, Y.-M. Chiang, High-performance battery electrodes via magnetic templating. *Nat Energy*. 1, 16099 (2016).

37. C. Lei, Z. Xie, K. Wu, Q. Fu, Controlled Vertically Aligned Structures in Polymer Composites: Natural Inspiration, Structural Processing, and Functional Application. *Adv Mater*. 33, e2103495 (2021).

38. J. C. da Silva, A. Pacureanu, Y. Yang, S. Bohic, C. Morawe, R. Barrett, P. Cloetens, Efficient concentration of high-energy x-rays for diffraction-limited imaging resolution. *Optica*. 4, 492 (2017).

39. P. Cloetens, W. Ludwig, J. Baruchel, D. V. Dyck, J. V. Landuyt, J. P. Guigay, M. Schlenker, Holotomography: Quantitative phase tomography with micrometer resolution using hard synchrotron radiation x rays. *Appl Phys Lett*. 75, 2912–2914 (1999).

40. A. Mirone, E. Brun, E. Gouillart, P. Tafforeau, J. Kieffer, The PyHST2 hybrid distributed code for high speed tomographic reconstruction with iterative reconstruction and a priori knowledge capabilities. *Nucl Instruments Methods Phys Res Sect B Beam Interactions Mater Atoms*. 324, 41–48 (2014).

41. U. Schmidt, M. Weigert, C. Broaddus, G. Myers, in *International Conference on Medical Image Computing and Computer-Assisted Intervention* (2018), *Lecture Notes in Computer Science*, pp. 265–273.

42. O. Ronneberger, P. Fischer, T. Brox, in *Medical Image Computing and Computer-Assisted Intervention* (2015), *arXiv*, pp. 234–241.

Author contributions: Y. Liu, K. Zhao, and F. Lin conceived the study. Y. Yang, F. Monaco, Z. Xu participated in performing synchrotron experiments and data processing. Z. Xu, D. Hou and F. Lin performed materials synthesis and electrochemistry. J. Li and Z. Jiang carried out the analysis of the experimental data. N. Sharma and K. Zhao performed the theoretical modeling. J. Li, N. Sharma, K. Zhao, F. Lin and Y. Liu wrote the manuscript with

valuable inputs from all coauthors. P. Pianetta, D. Ratner, and P. Cloetens contributed to the interpretation of the data and results. J. Li and N. Sharma contributed equally to this work.

Competing interests: Authors declare that they have no competing interests.

Data and materials availability: The source code supporting the findings of the study is available at https://doi.org/10.5281/zenodo.5888945.

Supplementary Materials

Materials and Methods

Figs. S1 to S12

References (*38*-*42*)

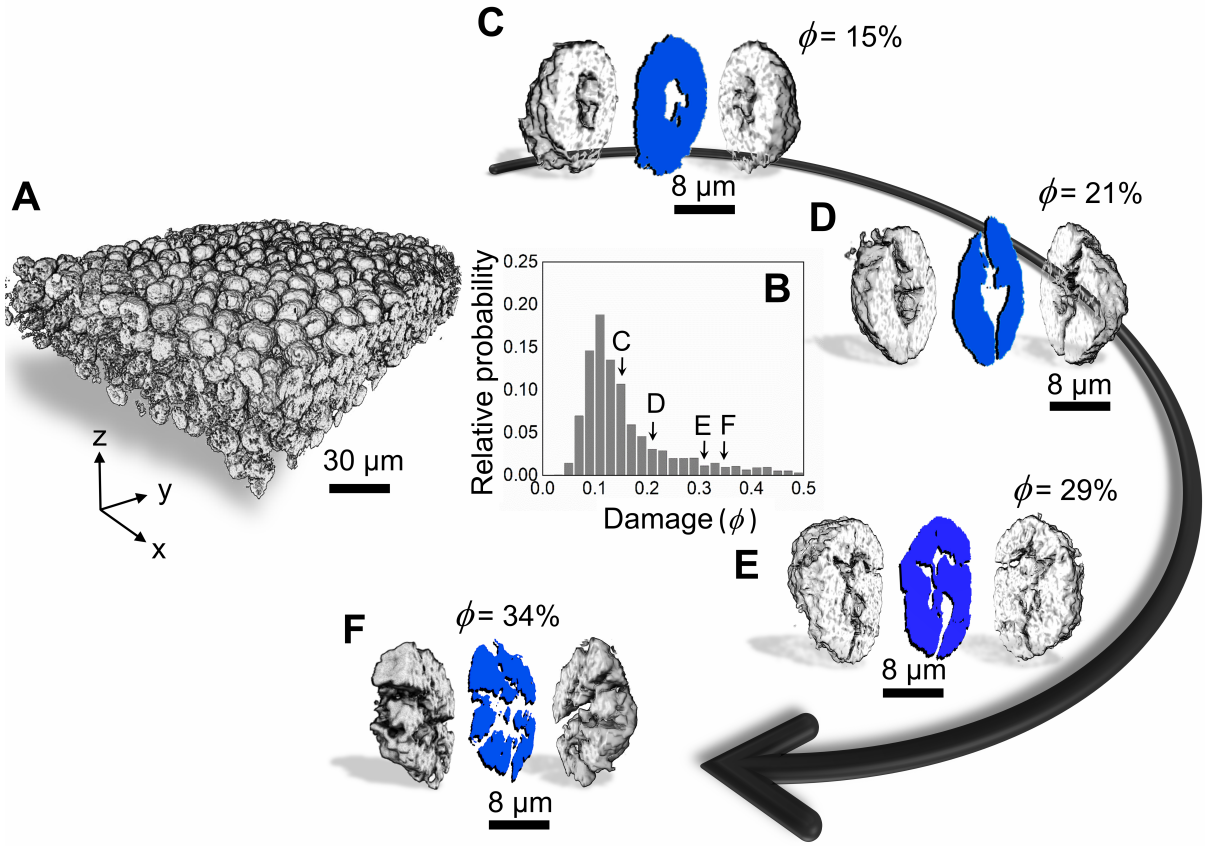

Fig. 1. Imaging cathode electrodes with multi-layer of NMC particles using nano-holo-tomography. (**A**) Visualization of the composite battery cathode obtained by synchrotron nano-holo-tomography. Each NMC particle has its own properties in position, particle structure, mesoscale chemistry, and local morphology. (**B**) Probability distribution of the particle porosity. (**C-F**) Randomly selected examples of NMC particles with different levels of damage.

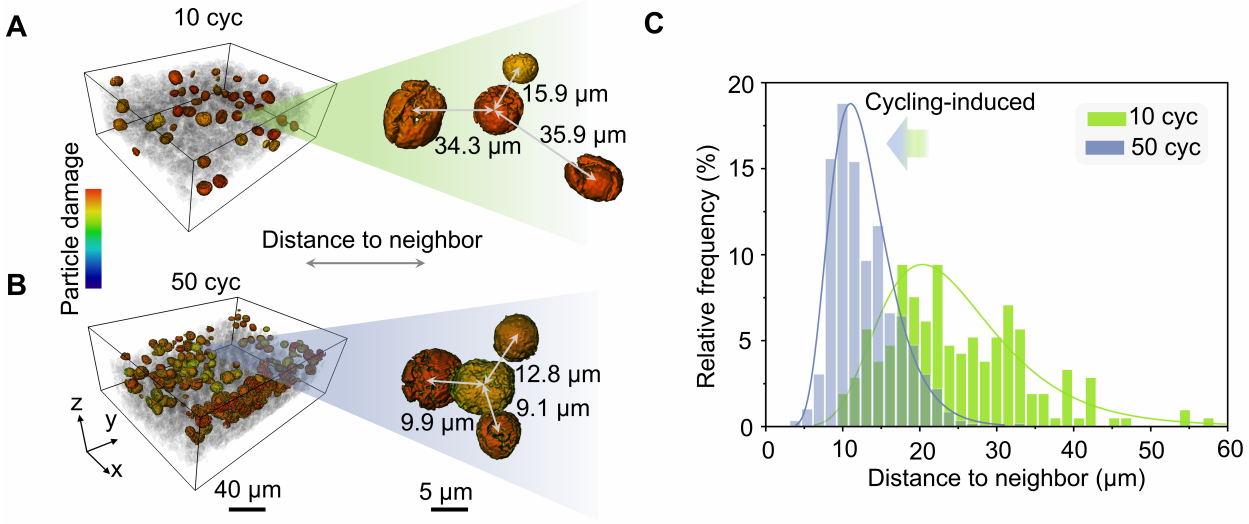

Fig. 2. **Particle damage heterogeneous in battery electrodes.** (**A-B**) The spatial distributions of the severely damaged particles in the 10-cycled and 50-cycled electrodes, respectively. The degree of particle damage is color coded. Selected representative regions are enlarged for better visualization. The distances between the central damaged particle to its three nearest neighboring damaged particles are annotated in the enlarged view. (**C**) Probability distributions of the distance between two neighboring severely damaged particles in 10-cycled and 50-cycled electrodes.

Fig. 3. Finite element analysis of the electrochemical activity and mechanical damage in the NMC cathode. (**A**) The illustration of the composite model during charging process in the battery. (**B**) Normalized Li concentration profiles depict the inherent heterogeneity of the system during the first charging process with respect to the normalized time , where is the real time in Li reactions and is the theoretical time to reach the full capacity of NMC. Although the particles start with the same state of charge, Li concentration differs at the end of the first charge process. (**C**) The variation of Li concentration profiles among three NMC particles. The overall trend demonstrates the tendency towards a synchronized behavior. (**D**) The damage profiles for three NMC active particles diverge near the end of the first charge process. With the progression of the cycling processes, the damage profiles for all three particles converge. (**E**) Each particle's deviation from the mean damage profile (the black dashed line).

Fig. 4. **Interpretable machine learning framework for particle attributes modeling.** (**A-B**) The Circular plots of the correlations of 9 latent dimensions (LDs) in 10-cycled and 50-cycled electrodes. The "+" and "-" signs denote positive and negative correlation, respectively. The correlations common to both electrodes are set semi-transparent while the different ones are highlighted. (**C**) The contribution scores of all attributes to the particle damage in 10-cycled (green) and 50-cycled (blue) electrodes. Triangle and square markers represent results from two robustness validation approaches, data-subsampling and random-seeding, respectively. The mean and standard deviation of the differences in the contribution scores (N = 20) between the 10-cycled and 50-cycled data are plotted on the top.